

1

CAMPINAS STATE UNIVERSITY

2

DOCTORAL THESIS

3

4 **Search of Z and Higgs boson decaying into $\Upsilon + \gamma$
5 in pp collisions at CMS/LHC**

6

7 *Author:*

Felipe Torres da Silva de Araujo

Supervisor:

Dr. José Augusto Chinellato

Co-Supervisor:

Dr. Alberto Franco de Sá Santoro

8

*A thesis submitted in fulfillment of the requirements
9 for the degree of Doctor of Physics*

10

in the

11

Graduate Program of
12 "Gleb Wataghin" Institute of Physics

13

September 27, 2020

14 “Sometimes science is a lot more art than science. A lot of people don’t get that.”

15

Rick Sanchez

16 “Então, que seja doce. Repito todas as manhãs, ao abrir as janelas para deixar entrar o sol ou o
17 cinza dos dias, bem assim, que seja doce. Quando há sol, e esse sol bate na minha cara amassada do
18 sono ou da insônia, contemplando as partículas de poeira soltas no ar, feito um pequeno universo;
19 repito sete vezes para dar sorte: que seja doce que seja doce que seja doce e assim por diante. Mas,
20 se alguém me perguntasse o que deverá ser doce, talvez não saiba responder. Tudo é tão vago como
21 se fosse nada.”

22

Caio Fernando Abreu

23 CAMPINAS STATE UNIVERSITY

24 *Abstract*

25 "Gleb Wataghin" Institute of Physics

26 Doctor of Physics

27 **Search of Z and Higgs boson decaying into $\Upsilon + \gamma$ in pp collisions at CMS/LHC**

28 by Felipe Torres da Silva de Araujo

29 This thesis presents the study on searches for rare decays of Standard Model bosons to quarkonia.
30 The searches are performed on data collected during the 2016 data taking of the CMS detector, at
31 center-of-mass energy $\sqrt{s} = 13$ TeV. Standard Model Higgs and Z bosons decaying to a $\Upsilon(1S, 2S, 3S)$
32 and a photon, with subsequent decay of the $\Upsilon(1S, 2S, 3S)$ to $\mu^+ \mu^-$ are performed using integrated
33 luminosity of 35.86 fb^{-1} from proton-proton collisions. No significant excess above the background-
34 only assumption is observed. A limit at 95% confidence level, is set on the $H \rightarrow \Upsilon(1S, 2S, 3S) + \gamma$
35 decay branching fraction at $(6.8, 7.1, 6.0) \times 10^{-4}$ and on $Z \rightarrow \Upsilon(1S, 2S, 3S) + \gamma$ decay branching
36 fraction at $(2.6, 2.3, 1.3) \times 10^{-6}$, using the CL_s method. Contributions given from 2016 to 2018 to
37 the operation, maintenance and R&D for Phase-2 Upgrade of Resistive Plate Chambers (RPC) at
38 CMS are also presented.

DRAFT

39

Acknowledgements

40 I would like to thank:

- 41 • the Campinas State University for providing the institutional support for this study;
- 42 • the Rio de Janeiro State University for the cooperation with Campinas State University in
43 their high-energy physics program. This was a key factor for this study;
- 44 • the National Council for Scientific and Technological Development (CNPq) for the financial
45 support for this work;
- 46 • the European Laboratory for Particle Physics (CERN) for the construction and operation of
47 the Large Hadron Collider (LHC);
- 48 • the Compact Muon Solenoid (CMS) collaboration for the construction, operation and provi-
49 sion of the instrumental means for this study.

DRAFT

50 Todo list

51	FAZER!	3
52	FAZER!	5
53	FAZER!	5
54	FAZER!	6
55	FAZER!	6
56	FAZER!	6
57	FAZER!	6
58	FAZER!	7
59	FAZER!	7
60	FAZER!	7
61	FAZER!	7

DRAFT

62 Contents

63	Abstract	iii
64	Acknowledgements	v
65	1 Experimental Setup	1
66	1.1 The Large Hadron Collider	1
67	1.2 The Compact Muon Solenoid - CMS	3
68	1.2.1 Coordinate system	4
69	1.3 Tracker	5
70	1.4 Electromagnetic Calorimeter	5
71	1.5 Hadronic Calorimeter	6
72	1.6 Muon System	6
73	1.6.1 DT	6
74	1.6.2 CSC	6
75	1.6.3 RPC	7
76	1.6.4 GEN	7
77	1.7 Trigger and Data Acquisition	7
78	1.8 Simulation, reconstruction and computing	7
79	1.9 Particle Flow Algorithm	7
80	Bibliography	11

DRAFT

⁸¹ List of Figures

⁸² 1.1	The LHC is the last ring (dark grey line) in a complex chain of particle accelerators. The smaller machines are used in a chain to help boost the particles to their final energies and provide beams to a whole set of smaller experiments. Source: [5].	⁸³ 2
⁸⁴ 1.2	Overview of the CMS experiment and its subdetectors. Source: [12].	⁸⁵ 4

DRAFT

⁸⁶ List of Tables

DRAFT

DRAFT

⁸⁷ 1 Experimental Setup

⁸⁸ This chapter describes the experimental setup used in this study, for the sake of brevity, it is provided
⁸⁹ a brief descriptions of the Large Hadron Collider (LHC), the Compact Muons Solenoid (CMS), and
⁹⁰ its subdetectors, and the process of high-level physics objects processing and reconstruction.

⁹¹ 1.1 The Large Hadron Collider

⁹² The Large Hadron Collider (LHC) is the world largest and powerful particle accelerator for protons
⁹³ and heavy-ions ever build. It is located in a complex of other accelerator operated by the European
⁹⁴ Organization for Nuclear Research (CERN), in the border of between Switzerland and France.
⁹⁵ The LHC is built in the same 26.7 km extension tunnel with depth varying from 45 m to 170
⁹⁶ m below the surface (the LHC plane is tilted 1.4% for construction reasons), once used by Large
⁹⁷ Electron–Positron Collider. The CERN complex is a composition of many accelerators, for proton
⁹⁸ and heavy-ions, used to provide beams of particles for smaller experiments and as a sequence of
⁹⁹ injectors for the LHC. Figure 1.1 presents the many components of the LHC complex of accelerators.
¹⁰⁰ A detailed description of the LHC can be found at [1–4].

¹⁰¹ A LHC section is composed of two vacuum pipes, in which the bunch of particles travels in opposite
¹⁰² directions. This means that both beams are magnetically coupled by the same super-conducting
¹⁰³ magnetic system, saving space and allowing the use of the pre-built LEP tunnel. The particle
¹⁰⁴ acceleration is made by Resonant Cavities [6]. Those cavities apply to each beam a set of radio-
¹⁰⁵ frequencies (RF) used to transfer energy by means of a 2 MV electric potential per cavity, at a
¹⁰⁶ revolution frequency of 400.789 MHz. The acceleration is applied to bunches of particles. The
¹⁰⁷ bunch configuration depends of the injection mode (configurable), but a typical pp injection would
¹⁰⁸ be composed by 2808 bunches of 1.1×10^{11} protons each. Proper timing of the bunches injection
¹⁰⁹ and the RF is a key factor for an efficient energy transfer inside the RF cavities. The cavities also
¹¹⁰ are operated in low temperatures of 4.5 K, to ensure superconducting properties and reduce energy
¹¹¹ losses.

¹¹² The nominal time spacing between each bunch (bunch crossing - BX) is 25 ns. This defines the
¹¹³ clock frequency of the LHC at $f_{LHC} = 400$ MHz. This frequency is propagated to all experiments
¹¹⁴ and used as a reference for timing and synchronization.

¹¹⁵ In certain positions, called the interaction points (IP), those two bunches are allowed to cross, possi-
¹¹⁶ bility the particle collisions. The experiments on the LHC are located in those interaction points.
¹¹⁷ ATLAS (A Toroidal LHC ApparatuS) [7] and CMS (Compact Muon Solenoid, better explained

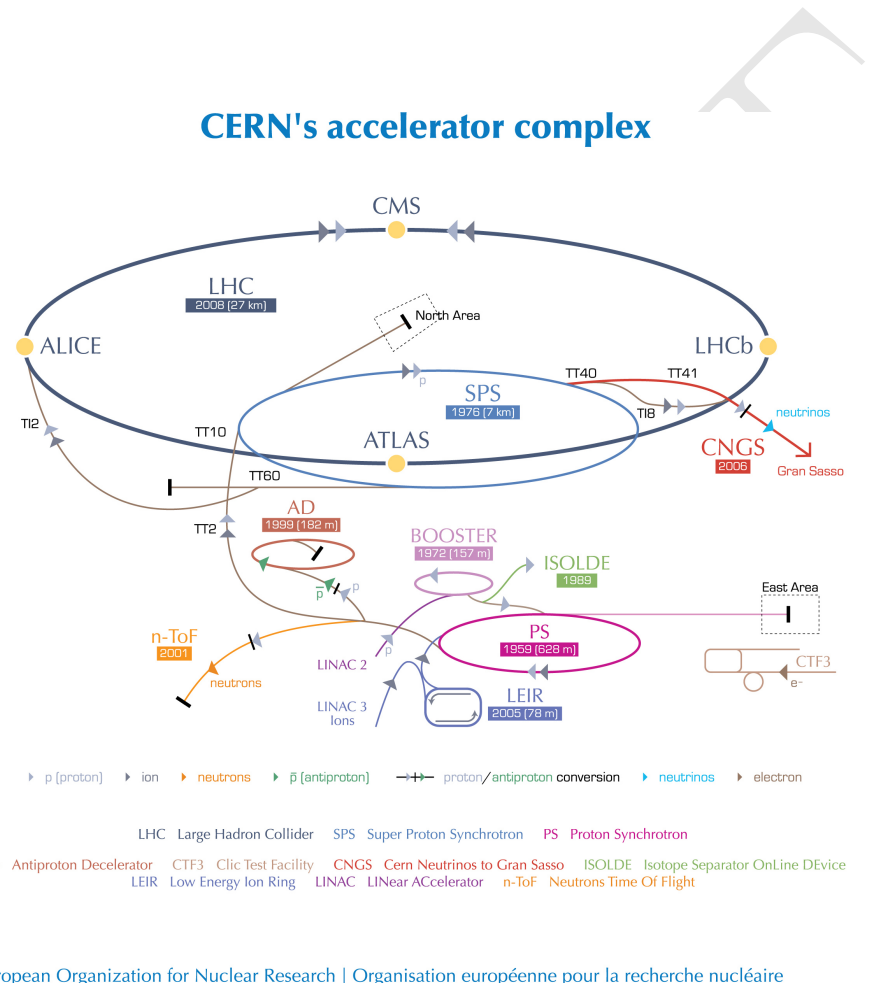


Figure 1.1: The LHC is the last ring (dark grey line) in a complex chain of particle accelerators. The smaller machines are used in a chain to help boost the particles to their final energies and provide beams to a whole set of smaller experiments. Source: [5].

in the next section), at P1 and P5, respectively, are so called general proposes experiments, with focus on different aspects of a particle interactions in the LHC energy scale, including extensive test of known Standard Model process (in high and low transverse momentum regime), including the Higgs sector and Heavy Flavour Physics (phenomena involving the hadrons composed by c and b quarks), exploration of Beyond Standard Model (BSM) phenomena, as well as an competitive program in heavy-ions collisions. The LHCb (Large Hadron Collider beauty) [8] is a experiment devoted, mostly, to precision measurements of CP violation and rare decays of B hadrons. The ALICE (A Large Ion Collider Experiment) [9] experiment is dedicated to the study of $p\text{-}Pb$ and $Pb\text{-}Pb$ collisions and processes such as QCD, strongly interacting matter and the quark-gluon plasma at extreme values of energy density and temperature.

The number of events of a certain kind i , per unit of time, is given by Equation 1.1.

$$\frac{dN^i}{dt} = \sigma^i \mathcal{L}, \quad (1.1)$$

where σ^i is the cross-section for a certain process i and \mathcal{L} is the instantaneous luminosity delivered by the LHC.

In order to accumulate as much statistics as possible, in the shortest amount of time (for the most efficiently use of the resources available, including person-power), the luminosity is a key factor in the exploration of the collisions. This is dependent of the number of particles per bunch, number of bunches per beam, revolution frequency, form factors of the bunches, crossing angles at the interaction points and correction factors to address relativistic and electromagnetic associated phenomena. For pp collisions, the LHC aims peak luminosities of, for ATLAS and CMS, around $2 \times 10^{34} \text{ cm}^{-2} \text{ s}^{-1}$. For future upgrades of the LHC (called HL-LHC [10]), the peak luminosity might increase 10 times, allowing an accumulated luminosity ¹ of 3000 fb^{-1} .

The LHC can collide protons with center-of-mass energy \sqrt{s} up to 14 TeV. Different energy configurations have been used so far, historically increasing the energy. For the operation cycle used in this study (Run2, from 2015 to 2018), the machine was producing collisions at $\sqrt{s} = 13 \text{ TeV}$. For the next operation cycle (Run3), to start in 2022, it is expected that the LHC might reach the 14 TeV energy values.

1.2 The Compact Muon Solenoid - CMS

FAZER!

The Compact Muon Solenoid (CMS) is a multiple purpose experiment used to investigated pp as well as lead-lead collisions at the LHC. It is operated by the CMS Collaborations, composed by around 5000 researches and 20 institutes ². The CMS is located in the city of Cessy, France, 100 below the surface. The CMS apparatus has an overall length of 22 m, a diameter of 15 m, and

¹Accumulated (or integrated) luminosity is defined as $L = \int \mathcal{L} dt$.

²It is important to stress that CMS is a collaboration of institutes, not researches.

150 weighs 14 000 tonnes. A detailed description of the CMS detector, can be found in [11]. Figure 1.2
 151 presents a sketch of CMS and its subdetectors.

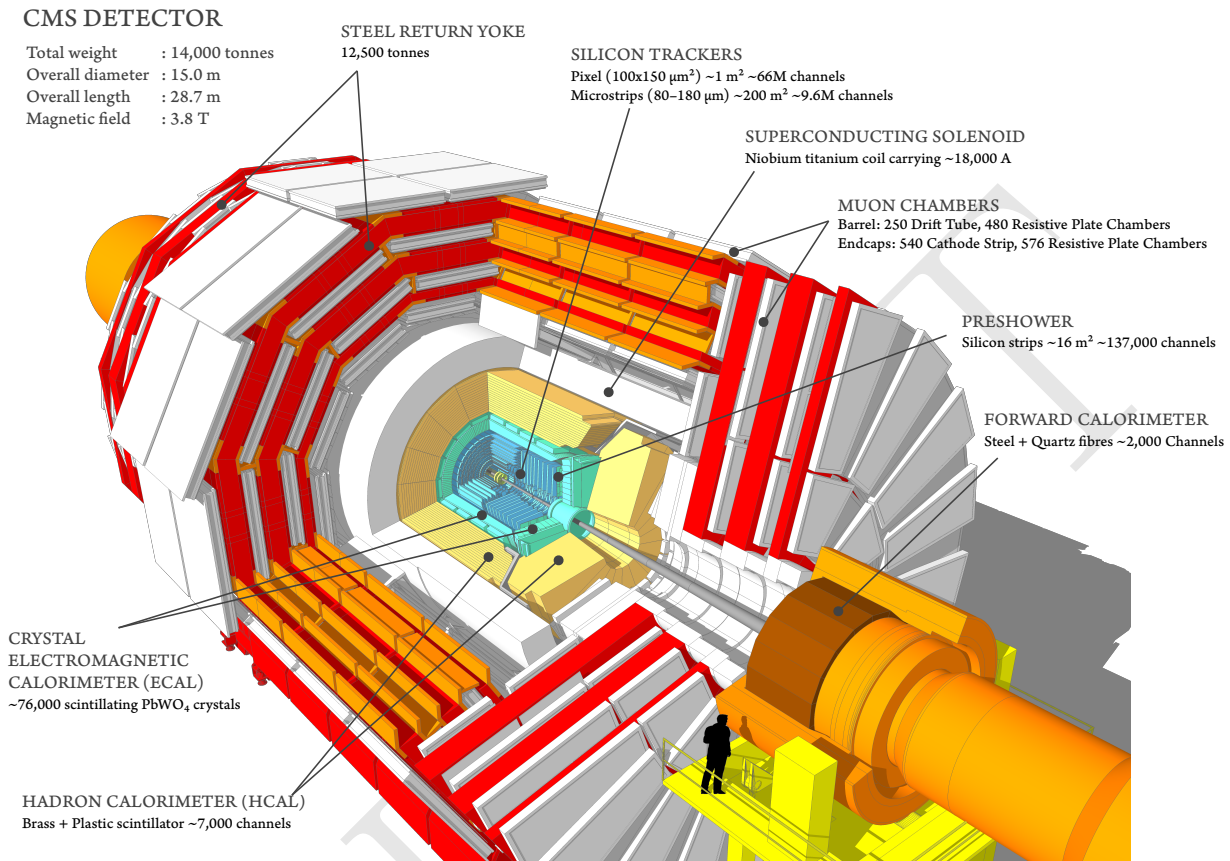


Figure 1.2: Overview of the CMS experiment and its subdetectors. Source: [12].

152 The central feature of the CMS apparatus is a superconducting solenoid of 6 m internal diameter,
 153 providing a magnetic field of 3.8 T. Within the solenoid volume are a silicon pixel and strip tracker,
 154 a lead tungstate crystal electromagnetic calorimeter (ECAL), and a brass and scintillator hadron
 155 calorimeter (HCAL), each composed of a barrel and two endcap sections. Forward calorimeters ex-
 156 tend the pseudorapidity coverage provided by the barrel and endcap detectors. Muons are detected
 157 in gas-ionization chambers embedded in the steel flux-return yoke outside the solenoid.

158 1.2.1 Coordinate system

159 CMS uses a right-handed coordinate system, with the origin at the nominal interaction point, the
 160 x axis pointing to the centre of the LHC ring, the y axis pointing up (perpendicular to the LHC
 161 plane), and the z axis along the anticlockwise-beam direction. The polar angle θ is measured from
 162 the positive z axis and the azimuthal angle ϕ is measured in the x - y plane.

163 It is important to define some key variables for CMS, in this study. The rapidity is defined as in
164 Equation 1.2, bellow.

$$y = \frac{1}{2} \ln \left(\frac{E + p_z}{E - p_z} \right), \quad (1.2)$$

165 where E is the energy of the object and p_z is the momentum ov the objects along the z direction.
166 The difference between the rapidity of two objects is known for being a lorentz invariant under a
167 boost.

168 A usually more suitable variable is the pseudorapidity, which is the rapidity in the relativistic limit
169 of $E \gg m$.

$$\eta = -\ln \left[\tan \left(\frac{\theta}{2} \right) \right], \quad (1.3)$$

170 where θ is the angle between the transverse plane to the beam line (x - y plane) and the positive z
171 direction. The convenience of using the pseudorapidity is its direct connection with the geometry
172 of the event by the θ angle.

173 1.3 Tracker

174 FAZER!

175 The silicon tracker measures charged particles within the pseudorapidity range $|\eta| < 2.5$. It consists
176 of 1440 silicon pixel and 15 148 silicon strip detector modules. For non-isolated particles of $1 <$
177 $p_T < 10 \text{ GeV}$ and $|\eta| < 1.4$, the track resolutions are typically 1.5% in p_T and 25–90 (45–150) μm
178 in the transverse (longitudinal) impact parameter [13].

179 1.4 Electromagnetic Calorimeter

180 FAZER!

181 The ECAL consists of 75 848 lead tungstate crystals, which provide coverage in pseudorapidity
182 $|\eta| < 1.48$ in a barrel region (EB) and $1.48 < |\eta| < 3.0$ in two endcap regions (EE). Preshower
183 detectors consisting of two planes of silicon sensors interleaved with a total of $3X_0$ of lead are
184 located in front of each EE detector [14]. In the barrel section of the ECAL, an energy resolution of
185 about 1% is achieved for unconverted or late-converting photons that have energies in the range of
186 tens of GeV. The remaining barrel photons have a resolution of about 1.3% up to a pseudorapidity
187 of $|\eta| = 1$, rising to about 2.5% at $|\eta| = 1.4$. In the endcaps, the resolution of unconverted or late-
188 converting photons is about 2.5%, while the remaining endcap photons have a resolution between
189 3 and 4% [15]. When combining information from the entire detector, the jet energy resolution
190 amounts typically to 15% at 10 GeV, 8% at 100 GeV, and 4% at 1 TeV, to be compared to about
191 40%, 12%, and 5% obtained when the ECAL and HCAL calorimeters alone are used.

192 **1.5 Hadronic Calorimeter**

193 FAZER!

194 In the region $|\eta| < 1.74$, the HCAL cells have widths of 0.087 in pseudorapidity and 0.087 in azimuth
 195 (ϕ). In the η - ϕ plane, and for $|\eta| < 1.48$, the HCAL cells map on to 5×5 arrays of ECAL crystals
 196 to form calorimeter towers projecting radially outwards from close to the nominal interaction point.
 197 For $|\eta| > 1.74$, the coverage of the towers increases progressively to a maximum of 0.174 in $\Delta\eta$ and
 198 $\Delta\phi$. Within each tower, the energy deposits in ECAL and HCAL cells are summed to define the
 199 calorimeter tower energies, which are subsequently used to provide the energies and directions of
 200 hadronic jets.

201 Jets are reconstructed offline from the energy deposits in the calorimeter towers, clustered using the
 202 anti- k_T algorithm [16, 17] with a distance parameter of 0.4. In this process, the contribution from
 203 each calorimeter tower is assigned a momentum, the absolute value and the direction of which are
 204 given by the energy measured in the tower, and the coordinates of the tower. The raw jet energy
 205 is obtained from the sum of the tower energies, and the raw jet momentum by the vectorial sum of
 206 the tower momenta, which results in a nonzero jet mass. The raw jet energies are then corrected to
 207 establish a relative uniform response of the calorimeter in η and a calibrated absolute response in
 208 transverse momentum p_T .

209 **1.6 Muon System**

210 FAZER!

211 Muons are measured in the pseudorapidity range $|\eta| < 2.4$, with detection planes made using three
 212 technologies: drift tubes, cathode strip chambers, and resistive plate chambers. The single muon
 213 trigger efficiency exceeds 90% over the full η range, and the efficiency to reconstruct and identify
 214 muons is greater than 96%. Matching muons to tracks measured in the silicon tracker results in
 215 a relative transverse momentum resolution, for muons with p_T up to 100 GeV, of 1% in the barrel
 216 and 3% in the endcaps. The p_T resolution in the barrel is better than 7% for muons with p_T up to
 217 1 TeV [18].

218 The muon detection system has nearly 1 million electronic channels.

219 **1.6.1 DT**

220 FAZER!

221 **1.6.2 CSC**

222 FAZER!

223 1.6.3 RPC

224 Due to the particularities of the study, especially the contributions given to the RPC project of
225 CMS, chapter ?? is devoted exclusively to this sub-detector.

226 1.6.4 GEN

227 FAZER!

228 1.7 Trigger and Data Acquisition

229 FAZER!

230 A two-tiered trigger system [19]. The first level (L1), composed of custom hardware processors, uses
231 information from the calorimeters and muon detectors to select events at a rate of around 100 kHz
232 within a time interval of less than $4\ \mu\text{s}$. The second level, known as the high-level trigger (HLT),
233 consists of a farm of processors running a version of the full event reconstruction software optimized
234 for fast processing, and reduces the event rate to around 1 kHz before data storage.

235 1.8 Simulation, reconstruction and computing

236 FAZER!

237 1.9 Particle Flow Algorithm

238 FAZER!

239 The global event reconstruction (also called particle-flow event reconstruction [20]) aims to re-
240 construct and identify each individual particle in an event, with an optimized combination of all
241 subdetector information. In this process, the identification of the particle type (photon, electron,
242 muon, charged hadron, neutral hadron) plays an important role in the determination of the par-
243 ticle direction and energy. Photons (e/γ coming from Z decays or from electron bremsstrahlung)
244 are identified as ECAL energy clusters not linked to the extrapolation of any charged particle tra-
245 jectory to the ECAL. Electrons are identified as a primary charged particle track and potentially
246 many ECAL energy clusters corresponding to this track extrapolation to the ECAL and to possible
247 bremsstrahlung photons emitted along the way through the tracker material. Muons are identified
248 as tracks in the central tracker consistent with either a track or several hits in the muon system, and
249 associated with calorimeter deposits compatible with the muon hypothesis. Charged hadrons are
250 identified as charged particle tracks neither identified as electrons, nor as muons. Finally, neutral
251 hadrons are identified as HCAL energy clusters not linked to any charged hadron trajectory, or as

252 a combined ECAL and HCAL energy excess with respect to the expected charged hadron energy
 253 deposit.

254 The energy of photons is obtained from the ECAL measurement. The energy of electrons is deter-
 255 mined from a combination of the track momentum at the main interaction vertex, the corresponding
 256 ECAL cluster energy, and the energy sum of all bremsstrahlung photons attached to the track. The
 257 energy of muons is obtained from the corresponding track momentum. The energy of charged
 258 hadrons is determined from a combination of the track momentum and the corresponding ECAL
 259 and HCAL energies, corrected for the response function of the calorimeters to hadronic showers.
 260 Finally, the energy of neutral hadrons is obtained from the corresponding corrected ECAL and
 261 HCAL energies.

262 The candidate vertex with the largest value of summed physics-object p_T^2 is taken to be the primary
 263 pp interaction vertex. For each event, hadronic jets are clustered from these reconstructed particles
 264 using the infrared and collinear safe anti- k_T algorithm [16, 17] with a distance parameter of 0.4. Jet
 265 momentum is determined as the vectorial sum of all particle momenta in the jet, and is found from
 266 simulation to be, on average, within 5 to 10% of the true momentum over the whole p_T spectrum
 267 and detector acceptance. Additional proton-proton interactions within the same or nearby bunch
 268 crossings (pileup) can contribute additional tracks and calorimetric energy depositions to the jet
 269 momentum. To mitigate this effect, charged particles identified to be originating from pileup vertices
 270 are discarded and an offset correction is applied to correct for remaining contributions. Jet energy
 271 corrections are derived from simulation to bring the measured response of jets to that of particle
 272 level jets on average. In situ measurements of the momentum balance in dijet, photon + jet, Z + jet,
 273 and multijet events are used to account for any residual differences in the jet energy scale between
 274 data and simulation [21]. The jet energy resolution amounts typically to 15–20% at 30 GeV, 10%
 275 at 100 GeV, and 5% at 1 TeV [21]. Additional selection criteria are applied to each jet to remove
 276 jets potentially dominated by anomalous contributions from various subdetector components or
 277 reconstruction failures.

278 Anomalous high- p_T^{miss} events can be due to a variety of reconstruction failures, detector malfunctions
 279 or non collisions backgrounds. Such events are rejected by event filters that are designed to identify
 280 more than 85–90% of the spurious high- p_T^{miss} events with a mistagging rate less than 0.1% [22].

281 Hadronic decays of top quarks are identified using the ratio between 3-subjettiness and 2-subjettiness [23],
 282 $\tau_{32} = \tau_3/\tau_2$, and the groomed jet mass. The groomed jet mass is calculated after applying a modified
 283 mass-drop algorithm [24, 25], known as the *soft drop* algorithm [26], to anti- k_T jets with a distance
 284 parameter of 0.8 and parameters $\beta = 0$, $z_{\text{cut}} = 0.1$, and $R_0 = 0.8$. The variables are calibrated in a
 285 top quark-antiquark enriched sample [27].

286 In the barrel section of the ECAL, an energy resolution of about 1% is achieved for unconverted
 287 or late-converting photons in the tens of GeV energy range. The remaining barrel photons have
 288 a resolution of about 1.3% up to a pseudorapidity of $|\eta| = 1$, rising to about 2.5% at $|\eta| = 1.4$.
 289 In the endcaps, the resolution of unconverted or late-converting photons is about 2.5%, while the
 290 remaining endcap photons have a resolution between 3 and 4% [15].

291 The electron momentum is estimated by combining the energy measurement in the ECAL with the
292 momentum measurement in the tracker. The momentum resolution for electrons with $p_T \approx 45$ GeV
293 from $Z \rightarrow ee$ decays ranges from 1.7% to 4.5%. It is generally better in the barrel region than in
294 the endcaps, and also depends on the bremsstrahlung energy emitted by the electron as it traverses
295 the material in front of the ECAL [14]."

DRAFT

DRAFT

²⁹⁶ Bibliography

- ²⁹⁷ [1] “LHC Machine”. In: *JINST* 3 (2008). Ed. by Lyndon Evans and Philip Bryant, S08001. doi:
²⁹⁸ 10.1088/1748-0221/3/08/S08001.
- ²⁹⁹ [2] Oliver Sim Brüning et al. *LHC Design Report*. CERN Yellow Reports: Monographs. Geneva:
³⁰⁰ CERN, 2004. doi: 10.5170/CERN-2004-003-V-1. URL: <http://cds.cern.ch/record/782076>.
- ³⁰² [3] Oliver Sim Brüning et al. *LHC Design Report*. CERN Yellow Reports: Monographs. Geneva:
³⁰³ CERN, 2004. doi: 10.5170/CERN-2004-003-V-2. URL: <http://cds.cern.ch/record/815187>.
- ³⁰⁵ [4] Michael Benedikt et al. *LHC Design Report*. CERN Yellow Reports: Monographs. Geneva:
³⁰⁶ CERN, 2004. doi: 10.5170/CERN-2004-003-V-3. URL: <http://cds.cern.ch/record/823808>.
- ³⁰⁸ [5] Christiane Lefèvre. “The CERN accelerator complex. Complexe des accélérateurs du CERN”.
³⁰⁹ Dec. 2008. URL: <http://cds.cern.ch/record/1260465>.
- ³¹⁰ [6] S Baird. *Accelerators for pedestrians; rev. version*. Tech. rep. AB-Note-2007-014. CERN-AB-
³¹¹ Note-2007-014. PS-OP-Note-95-17-Rev-2. CERN-PS-OP-Note-95-17-Rev-2. Geneva: CERN,
³¹² Feb. 2007. URL: <http://cds.cern.ch/record/1017689>.
- ³¹³ [7] The ATLAS Collaboration et al. “The ATLAS Experiment at the CERN Large Hadron Col-
³¹⁴ llider”. In: *Journal of Instrumentation* 3.08 (Aug. 2008), S08003–S08003. doi: 10.1088/1748-
³¹⁵ 0221/3/08/s08003. URL: <https://doi.org/10.1088%2F1748-0221%2F3%2F08%2Fs08003>.
- ³¹⁶ [8] Jr. Alves A. Augusto et al. “The LHCb Detector at the LHC”. In: *JINST* 3 (2008), S08005.
³¹⁷ doi: 10.1088/1748-0221/3/08/S08005.
- ³¹⁸ [9] K. Aamodt et al. “The ALICE experiment at the CERN LHC”. In: *JINST* 3 (2008), S08002.
³¹⁹ doi: 10.1088/1748-0221/3/08/S08002.
- ³²⁰ [10] “High-Luminosity Large Hadron Collider (HL-LHC): Technical Design Report V. 0.1”. In:
³²¹ 4/2017 (Nov. 2017). Ed. by G. Apollinari et al. doi: 10.23731/CYRM-2017-004.
- ³²² [11] S. Chatrchyan et al. “The CMS experiment at the CERN LHC”. In: *JINST* 3 (2008), S08004.
³²³ doi: 10.1088/1748-0221/3/08/S08004.
- ³²⁴ [12] Tai Sakuma. “Cutaway diagrams of CMS detector”. In: (May 2019). URL: <http://cds.cern.ch/record/2665537>.
- ³²⁶ [13] Serguei Chatrchyan et al. “Description and performance of track and primary-vertex recon-
³²⁷ struction with the CMS tracker”. In: *JINST* 9 (2014), P10009. doi: 10.1088/1748-0221/9/
³²⁸ 10/P10009. arXiv: 1405.6569 [physics.ins-det].

- [14] Vardan Khachatryan et al. “Performance of electron reconstruction and selection with the CMS detector in proton-proton collisions at $\sqrt{s} = 8$ TeV”. In: *JINST* 10 (2015), P06005. DOI: 10.1088/1748-0221/10/06/P06005. arXiv: 1502.02701 [physics.ins-det].
- [15] Vardan Khachatryan et al. “Performance of photon reconstruction and identification with the CMS detector in proton-proton collisions at $\sqrt{s} = 8$ TeV”. In: *JINST* 10 (2015), P08010. DOI: 10.1088/1748-0221/10/08/P08010. arXiv: 1502.02702 [physics.ins-det].
- [16] Matteo Cacciari, Gavin P. Salam, and Gregory Soyez. “The anti- k_t jet clustering algorithm”. In: *JHEP* 04 (2008), p. 063. DOI: 10.1088/1126-6708/2008/04/063. arXiv: 0802.1189 [hep-ex].
- [17] Matteo Cacciari, Gavin P. Salam, and Gregory Soyez. “FastJet User Manual”. In: *Eur. Phys. J.* C72 (2012), p. 1896. DOI: 10.1140/epjc/s10052-012-1896-2. arXiv: 1111.6097 [hep-ph].
- [18] A M Sirunyan et al. “Performance of the CMS muon detector and muon reconstruction with proton-proton collisions at $\sqrt{s} = 13$ TeV”. In: *JINST* 13 (2018), P06015. DOI: 10.1088/1748-0221/13/06/P06015. arXiv: 1804.04528 [physics.ins-det].
- [19] Vardan Khachatryan et al. “The CMS trigger system”. In: *JINST* 12 (2017), P01020. DOI: 10.1088/1748-0221/12/01/P01020. arXiv: 1609.02366 [physics.ins-det].
- [20] A. M. Sirunyan et al. “Particle-flow reconstruction and global event description with the CMS detector”. In: *JINST* 12 (2017), P10003. DOI: 10.1088/1748-0221/12/10/P10003. arXiv: 1706.04965 [physics.ins-det].
- [21] Vardan Khachatryan et al. “Jet energy scale and resolution in the CMS experiment in pp collisions at 8 TeV”. In: *JINST* 12 (2017), P02014. DOI: 10.1088/1748-0221/12/02/P02014. arXiv: 1607.03663 [hep-ex].
- [22] Albert M Sirunyan et al. “Performance of missing transverse momentum reconstruction in proton-proton collisions at $\sqrt{s} = 13$ TeV using the CMS detector”. In: *JINST* 14 (2019), P07004. DOI: 10.1088/1748-0221/14/07/P07004. arXiv: 1903.06078 [hep-ex].
- [23] Jesse Thaler and Ken Van Tilburg. “Identifying Boosted Objects with N -subjettiness”. In: *JHEP* 03 (2011), p. 015. DOI: 10.1007/JHEP03(2011)015. arXiv: 1011.2268 [hep-ph].
- [24] Mrinal Dasgupta et al. “Towards an understanding of jet substructure”. In: *JHEP* 09 (2013), p. 029. DOI: 10.1007/JHEP09(2013)029. arXiv: 1307.0007 [hep-ph].
- [25] Jonathan M. Butterworth et al. “Jet substructure as a new Higgs search channel at the LHC”. In: *Phys. Rev. Lett.* 100 (2008), p. 242001. DOI: 10.1103/PhysRevLett.100.242001. arXiv: 0802.2470 [hep-ph].
- [26] Andrew J. Larkoski et al. “Soft drop”. In: *JHEP* 05 (2014), p. 146. DOI: 10.1007/JHEP05(2014)146. arXiv: 1402.2657 [hep-ph].
- [27] Albert M Sirunyan et al. “Pileup mitigation at CMS in 13 TeV data”. In: *JINST* 15 (2020), P09018. DOI: 10.1088/1748-0221/15/09/p09018. arXiv: 2003.00503 [hep-ex].